Chemical Science

ROYAL SOCIETY OF CHEMISTRY

EDGE ARTICLE

View Article Online
View Journal | View Issue

Cite this: *Chem. Sci.*, 2020, **11**, 10225

All publication charges for this article have been paid for by the Royal Society of Chemistry

Selective active site placement in Lewis acid zeolites and implications for catalysis of oxygenated compounds

Aída Rodríguez-Fernández, †[a] John R. Di Iorio, †[b] Cecilia Paris, [a] Mercedes Boronat, [a] Avelino Corma, [a] Yuriy Román-Leshkov *[b] and Manuel Moliner *[a]

Received 12th July 2020
Accepted 7th September 2020

DOI: 10.1039/d0sc03809a

rsc.li/chemical-science

The selective incorporation of isolated framework Lewis acid sites at specific crystallographic positions in high-silica zeolites was achieved by applying a rationalized post-synthetic grafting methodology. The removal of framework Ge atoms from a Ge-BEC zeolite with low concentrations of Ge in the framework (Si/Ge ~ 150) followed by grafting allows the synthesis of Sn-BEC zeolites with Sn atoms positionally biased into the double-4-ring (D4R) crystallographic positions of the BEC framework. Spectroscopic characterization using solid-state nuclear magnetic resonance (NMR) coupled with theoretical calculations revealed that Sn atoms preferentially form open Sn sites in the D4R of Sn-BEC. This observation was supported by IR spectra of adsorbed deuterated acetonitrile (CD_3CN), a known titrant of Sn sites in zeolites. The catalytic implications of selective incorporation of open Sn sites in Sn-BEC were probed using the Meerwein–Ponndorf–Verley–Oppenauer (MPVO) reaction. Although the MPVO turnover rates normalized by the total number of open Sn sites were comparable on Sn-BEC and a conventional Sn-Beta catalyst synthesized in fluoride media (Sn-Beta(F)), Sn-BEC demonstrated higher per gram reaction rates because of its larger fraction of open sites compared to Sn-Beta(F). These results highlight the advantage of placing active sites in targeted locations within a zeolite structure. The methodology presented here to selectively place catalytic active sites *via* sacrificial heteroatoms, such as Ge, can be generalized for the design of many other tetrahedrally-coordinated metal-containing zeolites.

1. Introduction

Positioning catalytically active sites in predetermined positions within the framework of a zeolite is a powerful handle to modify catalytic activity and product selectivity.[1,2] The incorporation of trivalent heteroatoms, such as Al or B, into crystallographic T-site positions generates a negative charge on the zeolite framework, which must be adequately balanced in the final solid by an extra-framework inorganic or organic cation. Several direct synthetic approaches have leveraged this feature to bias the location of Al species in zeolite pores, cavities, and intersections by manipulating the size, shape and charges of the counterbalancing cations during hydrothermal synthesis.[1–11] Zeolites of a given framework topology can be synthesized with varied fractions of their framework Al atoms located in pores of different size using mixtures of different structure directing agents. Accordingly, the location of Al atoms within a zeolite alters reaction rates and selectivities, as demonstrated for a variety of acid catalysed reactions using positionally biased H-MFI (*e.g.*, olefin oligomerization,[12] alkane cracking,[10] and methanol conversion[9,13–15]) and H-FER (*e.g.*, isomerization,[4,16] alkane and alkene cracking,[6] and carbonylation[6]) zeolites. Moreover, the synthesis of organic structure directing agents (OSDAs) that mimic known transition states has also led to the design of tailored zeolite frameworks with enhanced reactivity for toluene disproportionation, isomerization, and methanol upgrading reactions.[17,18]

Incorporation of tetravalent heteroatoms with open coordination sites (*e.g.*, Ti, Sn, and Zr) into crystallographic framework positions gives rise to Lewis acid sites.[19–21] These catalysts are ideally suited to activate oxygenated molecules, showing exceptional selectivity and yields for the transformation of biomass-derived molecules.[22–24] For example, Sn-Beta—a catalyst featuring isolated tin sites incorporated into the Beta framework—has been extensively evaluated as the paradigmatic catalyst for many reactions of bio-derived molecules, including carbohydrate isomerization and epimerization, inter and intramolecular transfer hydrogenation, and aldol condensation.[25–30] However, unlike a trivalent heteroatom whose position

[a]*Instituto de Tecnología Química, Universitat Politècnica de València-Consejo Superior de Investigaciones Científicas, Avenida de los Naranjos s/n, 46022 València, Spain. E-mail: mmoliner@itq.upv.es*

[b]*Department of Chemical Engineering, Massachusetts Institute of Technology, 77 Massachusetts Ave, Cambridge, MA 02139, USA. E-mail: yroman@mit.edu*

† These authors have contributed equally.

within the zeolite framework can be directly influenced by electrostatic interactions with inorganic and organic cations, biasing the location of an isolated tetravalent Lewis acid site is difficult because charge balancing does not occur during crystallization. Consequently, directing these heteroatoms to specific crystallographic locations during zeolite synthesis has not been demonstrated using traditional synthetic approaches.

The ubiquitous use of the Beta topology to host Lewis acid sites originates from its synthetic versatility, as it is one of the few structures with large pores that can be prepared under a broad range of synthesis conditions with precise control over crystal size and heteroatom identity.[31,32] The crystalline structure of Beta is formed by the intergrowth of two different polymorphs, BEA and BEB (50 : 50 ratio), each featuring 9 distinct crystallographic tetrahedral sites (T-sites; Fig. 1a and b).[33] Using extended X-ray absorption fine structure (EXAFS) to elucidate the distribution of Sn across these T-sites, Corma and co-workers proposed preferential positioning of Sn atoms at the T_5 and T_6 sites (Fig. 1b) in Sn-Beta synthesized with fluoride media (Sn-Beta(F)).[34] Román-Leshkov *et al.* used solid-state magic angle spinning ^{31}P nuclear magnetic resonance (NMR) spectroscopy to identify several well-defined signals corresponding to the adsorption of trimethylphosphine oxide (TMPO) at different Sn sites in Beta zeolites, suggesting chemical diversity of such active sites. This work established correlations between different ^{31}P chemical shifts and the catalytic activity for the glucose isomerization and aldol condensation reactions.[35] Sn atoms have also been shown to adopt different coordination within Beta zeolites, namely "open" Sn sites, which contain three bonds to framework oxygen atoms and one hydroxyl ligand (*i.e.*, $Sn(OSi)_3$–OH), and "closed" Sn sites, which contain four bonds to framework oxygen atoms (*i.e.*, $Sn(OSi)_4$).[36] The number of open Sn sites has been shown to correlate with rates of Baeyer–Villiger oxidation and Meerwein–Ponndorf–Verley–Oppenauer (MPVO) reactions.[21,36] Recently, Gounder *et al.* have proposed that these open Sn sites are preferentially located at stacking faults present in Beta zeolites[37,38] that form from the intergrowth of both polymorphs during crystallization.[33,39,40] Despite these previous efforts, the precise assignment of Lewis acid sites distributed across the different T-sites in Beta zeolites remains under debate and the prospect of developing synthetic strategies to control the position of sites across 18 unique T-sites and framework defects remains obscure.

A third polymorph of Beta, BEC, holds promise to overcome these limitations. The BEC framework is formed by the same zeolitic layers comprising BEA and BEB, but these layers are stacked in a different arrangement, creating a three-dimensional large pore system with straight channels (Fig. 1c). Consequently, BEC contains only three distinct crystallographic T-sites (Fig. 1d), half of which are located in the double-4-ring (D4R) secondary building units. This feature was the key to synthesizing ITQ-17, the first BEC-type zeotype obtained experimentally.[41,42] Specifically, Ge heteroatoms were used in the synthesis media (Si/Ge ratio < 5) in combination with different OSDAs to crystallize BEC, surmising that Ge would be more adept than Si at accommodating the tight angles in the D4Rs. Recently, a Ge-rich Sn-BEC (Si/Ge = 5) was reported to selectively catalyze the isomerization of glucose to methyl fructoside in methanol,[43] unlike Sn-Beta, which converted glucose to methyl mannoside *via* both isomerization and epimerization pathways under identical reaction conditions (120 °C). This difference was ascribed to the preferential occupancy of isolated Lewis acid catalytic centers in the D4Rs of the BEC structure.[43] While promising, Ge-rich zeolites are hydrothermally unstable and readily undergo degermanation even in the presence of atmospheric water.[44] Although the labile nature of Ge species in zeolites has been recently employed to achieve novel zeolite structures through the assembly–disassembly–organisation–reassembly (ADOR) transformation methodology[45] and to create hybrid Ge-based electronic conductors,[46] framework collapse *via* degermanation is a major impediment to the development of stable catalytic materials.

Here, we present a strategy to generate stable Sn-BEC zeolites with positionally biased Lewis acid sites and investigate the catalytic implications of this approach. Prior reports demonstrated the cooperative effect between specific OSDA molecules (Fig. 2) and F incorporation within the D4Rs to generate pure-silica BEC without requiring the presence of Ge

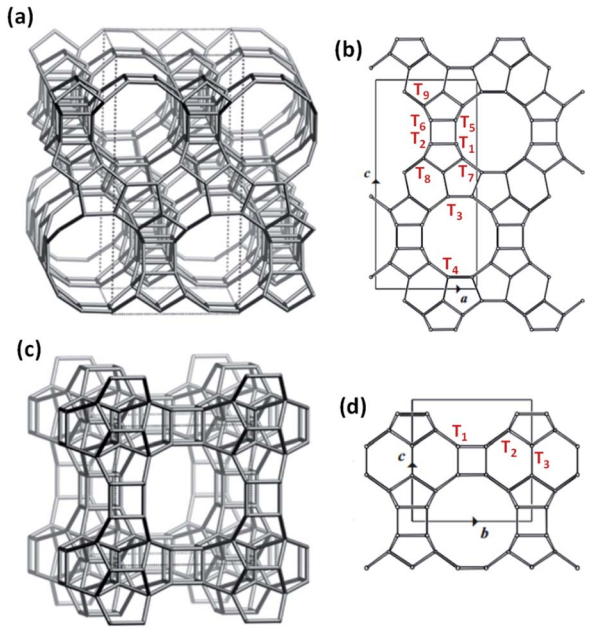

Fig. 1 Framework structures of BEA (a) and BEC (c) and the different crystallographic T-sites in the unit cell of BEA (b) and BEC (d).

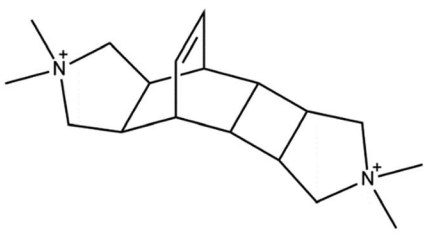

Fig. 2 OSDA employed for the synthesis of the high-silica BEC zeolite.

heteroatoms.[47] We build upon this strategy by generating BEC zeolites with low concentrations of framework Ge (Si/Ge > 150), hypothesizing that the limited number of Ge atoms per unit cell would be preferentially positioned in the D4Rs.[47,48] These Ge atoms can then be isomorphically substituted with Sn using simple post-synthetic treatments without jeopardizing the structural integrity of the zeolite framework. Given the strain at these locations, the Sn atoms preferentially exist in an open configuration, in agreement with the observations by Gounder and co-workers where a higher proportion of open sites was detected at strained stacking fault sites between Beta polymorphs.[37] NMR and FTIR spectroscopies confirmed the incorporation of Lewis acidic Sn species within the BEC framework that are located predominantly in a single crystallographic environment. Reactivity studies using MPVO as a probe reaction show that the Sn-BEC featured similar turnover rates (normalized per open Sn site) to classical Sn-Beta(F) catalysts, but showed higher reaction rates per gram of zeolite due to the larger number of open Sn sites on a mass basis. These results demonstrate that catalytic active sites can be selectively placed in targeted locations within a given zeolite structure by taking advantage of the preferential incorporation of sacrificial heteroatoms at specific crystallographic sites.

2. Experimental section

2.1. BEC-type zeolite syntheses

2.1.1. OSDA synthesis. The OSDA was synthesized as follows: 12 g of *N*-methylmaleimide (Sigma Aldrich, 97 wt%) was dissolved in 300 ml of benzene, followed by the addition of 30 ml of acetophenone (Sigma Aldrich, 99 wt%) and 84 ml of acetone. The resultant solution was distributed in 10 Pyrex glass tubes (50 ml), and N_2 was flowed through the solutions for 15 min before irradiating with a high-pressure Hg lamp ($200 < \lambda < 90$ nm) for 48 h under stirring. The precipitate was filtered under vacuum providing the desired diimide (37%). Then, a suspension of $LiAlH_4$ (244 mmol) in anhydrous THF (300 ml) was slowly added to the diimide (49 mmol) under N_2 at 0 °C. Afterwards, the mixture was refluxed for 5 h, cooled, and stirred at room temperature overnight. The reaction was quenched by sequential addition of distilled H_2O (10 ml), 15% aqueous solution of NaOH (10 ml), and distilled H_2O (10 ml). After stirring at room temperature for 30 min, the solution was filtered, partially concentrated by rotary evaporation, and then extracted with dichloromethane. The combined organic extracts were washed with brine, dried, and concentrated to dryness yielding the corresponding diamine (70%). Finally, 1.7 mol of CH_3I was added to a solution of the diamine (33.5 mmol) in methanol (85 ml), and maintained for 2 days under stirring at room temperature. The resultant precipitate was filtered and washed with diethyl ether and, finally, dried under high vacuum to obtain (4*R*,4a*R*,7a*S*,8*S*,8a*S*)-2,2,6,6-tetramethyl-1,2,3,3*a*,3*b*,4,4*a*,5,6,7,7*a*,8,8*a*,8*b*-tetradecahydro-4,8-ethenopyrrolo[3′,4′:3,4]cyclobuta[1,2-*f*]isoindole-2,6-diium iodide [75%, TMTEC(I)$_2$].

The iodide form of the organic salt was exchanged to the hydroxide form as follows: 24 mmol of the iodide salt was dissolved in water, adding 50 g of Dower-SBR Anion Exchange resin in hydroxide form (total exchange capacity 1.4 eq. l^{-1}) and maintaining the mixture under agitation overnight. The solution was filtered to obtain the dihydroxide cation [TMTEC(OH)$_2$] and titrated with HCl to confirm its purity.

2.1.2. Ge-BEC (Si/Ge ∼ 150). Ge-BEC zeolite was synthesized as follows: 20.00 g of a 7.7% wt aqueous solution of the TMTEC(OH)$_2$ was mixed with 3.04 g of Ludox AS-40 (Sigma-Aldrich) and 0.015 g of germanium oxide (Sigma-Aldrich). Then, 3.70 g of NH_4F solution (10% wt) was added to the gel, and the mixture was stirred until evaporation of the excess of water. The final composition of the gel was: SiO_2/0.0067GeO_2/0.25TMTEC(OH)$_2$/0.5NH_4F/2H_2O. The gel was heated at 175 °C in Teflon lined stainless steel autoclaves for different days, and the resultant solids were filtered, washed and dried at 100 °C. The material was calcined at 580 °C in air for 6 hours.

2.1.3. DeGe-BEC. The procedure to remove framework Ge atoms from the Ge-BEC solid was as follows: 0.5 g of calcined Ge-BEC zeolite was mixed with 45 ml of an aqueous HCl solution (0.01 M) and the resultant mixture was refluxed and stirred at 100 °C overnight. The solid was filtered, washed, and dried at 100 °C. The degermanized material, DeGe-BEC, was calcined at 580 °C in air for 6 hours.

2.1.4. Sn-BEC. First, DeGe-BEC zeolite was dehydrated under vacuum at 120 °C for 2 hours. Then, post-synthetic grafting of Sn was carried out using $SnCl_3CH_3$ (Sigma-Aldrich) with a theoretical molar ratio of Si/Sn of 100 in anhydrous chloroform (40 ml g^{-1} zeolite). Specifically, DeGe-BEC and $SnCl_3CH_3$ were added to chloroform and stirred for 1 h at room temperature. Next, triethylamine was added (3 mol triethylamine/mol chloroform) and the resultant mixture was stirred for two days at room temperature. The sample was washed with chloroform and water and dried at 100 °C overnight. Finally, the material was calcined at 580 °C in air for 6 hours.

2.2. Synthesis of Sn-Beta in fluoride media (Sn-Beta(F))

Sn-Beta(F) was synthesized following a previously reported procedure.[49] Briefly, 11.65 g of an aqueous solution of tetraethylammonium hydroxide (TEAOH; Sigma-Aldrich, 40 wt%) and 8.44 g of deionized water (18.2 MΩ) were added to a perfluoroalkoxy alkane (PFA, Savillex Corp.) jar and stirred under ambient conditions for 5 minutes to homogenize the contents. Next, 12.1 g of tetraethylorthosilicate (TEOS; Sigma-Aldrich, 99 wt%) was added to the aqueous TEAOH solution, and the mixture was covered and stirred under ambient conditions for 120 minutes. Then, 0.044 g of stannous chloride ($Sn(II)Cl_2$; Sigma-Aldrich, 98 wt%) was dissolved in ∼2 g of ethanol (Koptec, 99.5 wt%) and this mixture was added dropwise to the aqueous solution of TEAOH and TEOS. The resulting solution was left uncovered and stirred under ambient conditions to evaporate ethanol and excess water. After reaching the desired final mass, 1.30 g of hydrofluoric acid (HF; Sigma-Aldrich, 48 wt% in H_2O, ≥99.99% trace metals basis) was added dropwise and the mixture was manually stirred with a PTFE spatula for 5 minutes to homogenize the contents. The resulting molar

composition of the synthesis media was: $1SiO_2/0.0033SnO_2/0.54TEAOH/0.54HF/7.52H_2O$. The mixture was then seeded with 0.173 g of dealuminated Beta zeolite (5 wt% SiO_2 basis), transferred to a 45 ml PTFE-lined stainless steel autoclave (4744, Parr Instruments), and heated to 160 °C under rotation (~40 RPM) for 7 days. Solids were then recovered *via* centrifugation, washed repeatedly with deionized water and acetone (99.5 wt%, BDH Chemicals) until the pH of the supernatant remained constant between washes, and then dried at 100 °C overnight under ambient air. The dried solids were then heated to 580 °C under flowing air for 10 hours.

2.3. Characterization

2.3.1. General characterization techniques. Powder X-ray diffraction (PXRD) measurements were performed with a multisample Philips X'Pert diffractometer equipped with a graphite monochromator, operating at 40 kV and 35 mA, and using Cu Kα radiation ($\lambda = 0.1542$ nm).

Chemical analyses were carried out in a Varian 715-ES ICP-Optical Emission spectrometer, after solid dissolution in HNO_3/HCl/HF aqueous solution. Elemental analyses were performed by combustion analysis using a Eurovector EA 3000 CHNS analyzer.

The morphology of the samples was studied by field emission scanning electron microscopy (FESEM) using a ZEISS Ultra-55 microscope.

Diffuse reflectance ultraviolet-visible spectra were measured using an Agilent Cary 5000 spectrometer equipped with a UV-Vis DiffusIR environmental chamber (Pike Technologies). Zeolite powders were dehydrated by heating to 250 °C (5 °C min^{-1}) under flowing dry N_2 and held for 2 hours prior to cooling to 30 °C. Spectra were measured relative to a pure-silica Beta zeolite.

Solid-state NMR spectra were recorded at room temperature with a Bruker AV 400 MAS spectrometer. ^{29}Si magic angle spinning (MAS) NMR spectra were recorded with a spinning rate of 5 kHz at 79.459 MHz with a 55° pulse length of 3.5 μs and repetition time of 180 s. ^{19}F was measured at 376.28 MHz at 25 kHz with pulses of 4.5 μs corresponding to a flip angle of $\pi/2$ rad, and a recycle delay of 100 s to ensure the complete recovery of the magnetization. ^{29}Si and ^{19}F chemical shifts were referred to tetramethylsilane and $CFCl_3$, respectively.

2.3.2. Trimethylphosphine oxide (TMPO) adsorption combined with ^{31}P MAS NMR spectroscopy. Zeolite samples were first dehydrated at 120 °C under vacuum for 4 h and then transferred to a glovebox to prevent exposure to moisture. TMPO solutions were prepared with anhydrous dichloromethane in a glovebox, introducing the required content to achieve ~0.5 TMPO/metal ratio. The mixture was stirred overnight at room temperature. Dichloromethane was fully removed by heating at 120 °C under vacuum for 4 h. Samples dosed with TMPO were packed under inert atmosphere into zirconia MAS NMR rotors with gastight caps for analysis.

Solid-state ^{31}P MAS NMR spectra were recorded at room temperature under magic angle spinning in a Brucker AV-400 spectrometer at 161.9 MHz with a spinning rate of 10 kHz and $\pi/2$ pulse length of 3.7 μs with spinal proton decoupling and recycle delay of 20 s. The ^{31}P chemical shift was referred to phosphoric acid.

2.3.3. Quantification of open and closed Lewis acid sites: IR studies with deuterated acetonitrile. IR spectra were measured using a Bruker Vertex 70 spectrometer equipped with a Hg–Cd–Te (MCT) detector, cooled to −196 °C with liquid N_2, by averaging 128 scans at 4 cm^{-1} resolution between 4000 to 400 cm^{-1}. All IR spectra were measured relative to an empty cell background spectrum collected under dynamic vacuum at 30 °C. Sn-containing zeolites (~5–10 mg) were pressed into 7 mm diameter self-supporting discs, loaded into a Harrick high temperature transmission cell (Harrick Scientific Products Inc.), and sealed with KBr windows (32 × 3 mm; Harrick Scientific Products Inc.). The temperature of the transmission cell was measured by a thermocouple (K-type, 1/16″, Omega) inserted into the cell just below the sample in contact with the cell wall and controlled by a Watlow EZ-Zone control module. Both the cell inlet and outlet were connected to stainless steel bellows valves to allow for isolation and evacuation of the transmission cell. The inlet valve was then connected *via* 1/4″ flexible stainless steel tubing to a Schlenk Line (Chemglass Airfree), which enabled isolation of the vacuum manifold, pretreatment gas manifold, and dosing ampules. The outlet valve was connected to an oil bubbler to minimize backflow of ambient air into the cell.

Prior to collection of IR spectra, each sample was heated to 400 °C (2 °C min^{-1}) under flowing dry air (50 cm^3 min^{-1}) for 2 hours, cooled under flowing air to 30 °C, and evacuated until the pressure in the cell reached $<8.0 \times 10^{-5}$ torr (Edwards T-Station 75 Turbopump). Acetonitrile-d_3 (CD_3CN; anhydrous, ≥99.8 atom% D, Sigma-Aldrich) was purified *via* successive freeze–pump–thaw cycles to remove dissolved gases and volatiles, and then introduced to the cell in serial doses ($1.4–7.0 \times 10^{-7}$ mol per dose). An IR spectrum was measured after pressure in the cell remained constant for >30 seconds. The spectrum of the dehydrated parent zeolite was subtracted from all subsequent spectra after CD_3CN dosing, which were then baseline corrected and normalized by the total area of the Si–O–Si combination and overtones modes (2100 to 1750 cm^{-1}) of the parent zeolite sample. Assignments for CD_3CN coordinated to open Sn (ν(C≡N): 2316 cm^{-1}), closed Sn (2308 cm^{-1}), silanol groups (2275 cm^{-1}), and physisorbed or gas-phase CD_3CN (2265 cm^{-1}) are based on prior assignments.[36,38,50] The total number of Lewis acidic Sn sites and the fraction of Sn found in and closed coordination environments were quantified using reported integrated molar extinction coefficients and deconvolution methods.[38]

2.4. Meerwein–Ponndorf–Verley–Oppenauer (MPVO) reaction between cyclohexanone and 2-butanol

Rates of the MPVO reaction between cyclohexanone and 2-butanol were measured in glass batch reactors (10 cm^3, VWR) using reactant solutions containing 0.01–1 M cyclohexanone (99 wt%, Sigma-Aldrich) in 2-butanol (99.8 wt%, Sigma-Aldrich). A specific amount of catalyst (5–10 mg) and a PTFE coated

magnetic stir bar were loaded into a batch reactor and sealed with a PTFE/silicone septum in an aluminum crimp top (Ace Glass). 2 cm^3 of a reactant solution were added to a separate batch reactor, sealed with a PTFE/silicone septum, and both catalyst and reactant vessels were heated to 100 °C for >15 minutes. After the preheating step, the reactant solution was transferred to the catalyst vial *via* syringe and the reaction allowed to proceed under stirring (300 RPM) at 100 °C. Aliquots of the reactant solution were taken after ~5 minutes, quenched in an ice bath, and filtered through a 0.2 μm PTFE syringe filter (VWR). The filtered reactant solutions were then diluted with a 2-pentanone standard solution (5 wt% in 2-butanol; 99.5 wt%, HPLC grade, Sigma-Aldrich) and injected to a gas chromatograph (7890A, Agilent Technologies) equipped with a DB-1701 column (30 m × 250 μm × 0.25 μm, Agilent Technologies) and a flame ionization detector. Initial cyclohexanol formation rates (normalized per open Sn site) were determined by extrapolating transient cyclohexanol production (moles of cyclohexanol produced g_{cat}^{-1}) to zero reaction time (*i.e.*, zero conversion) using data measured at <10% conversion.

2.5. Computational details

The active sites in Sn-BEC and Sn-BEA catalysts were simulated by cluster models cut out from the respective periodic crystalline structures and containing one framework Sn atom per unit cell, either bonded to four O–Si units (*i.e.*, closed site) or with one hydrolyzed Sn–OH bond (*i.e.*, open site). The dangling bonds that connected the cluster with the rest of the solid were saturated with H atoms, and during geometry optimization these terminal H atoms were kept fixed to maintain the zeolite structure, while all other atoms in the model were allowed to relax without restrictions. Sn was placed at T_1, T_2 and T_3 positions in BEC, and at T_4, T_5 and T_7 positions in BEA. The three positions in BEA were selected according to the size of the rings they belong to: 4R and 5R for T_1, T_2, T_5 and T_6; 4R, 5R and 6R for T_3, T_4, T_8 and T_9; and only 5R in the case of T_7. All density functional theory (DFT) calculations were carried out using the M062X functional,[51] the 6-31g(d,p) basis set for O, C, P and H atoms,[52,53] and the LANL2DZ basis set and pseudopotential for Sn,[54,55] as implemented in the Gaussian09 software.[56] For the simulation of NMR parameters, the isotropic absolute chemical shielding constants (σ) were obtained using the gauge including atomic orbitals (GIAO) approach[57,58] and the ^{31}P chemical shifts were calculated as $\delta\ ^{31}P = \sigma_{ref} - \sigma$, using phosphoric acid as reference. To improve accuracy, all values were corrected with an equation obtained by fitting $\delta\ ^{31}P$ values at 6-31G(d,p) level against $\delta\ ^{31}P$ values at 6-311++G(d,p) level[59] for a series of acid–base TMPO adducts.

3. Results and discussion

3.1. Synthesis of Sn-containing BEC

The strategy used to generate positionally biased Sn-BEC samples using post-synthetic grafting of degermanized BEC samples is depicted in Fig. 3. Prior reports confirmed that Ge heteroatoms preferentially occupy T-sites in the D4Rs before populating other sites within the zeolite.[42,44] A Si/Ge molar ratio of 150 was selected because it is similar to the Si/Sn content

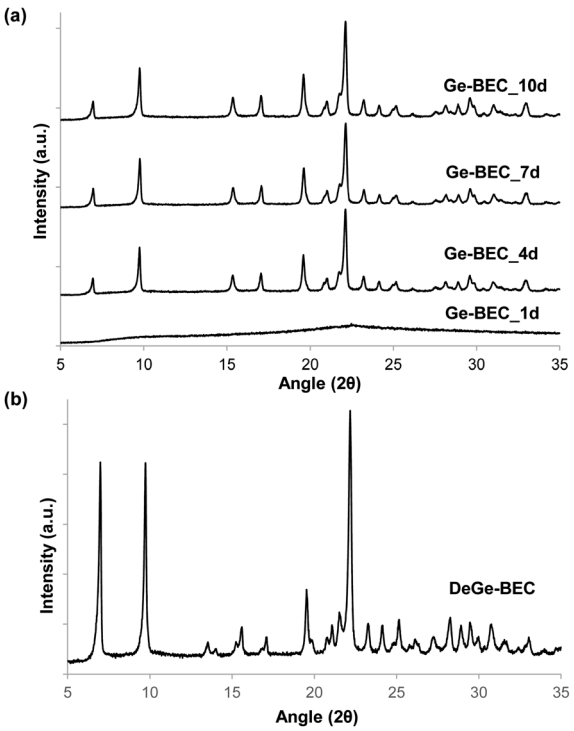

Fig. 4 PXRD patterns of (a) Ge-BEC taken at different crystallization times (1–10 days) with a Si/Ge molar ratio of 150 and (b) degermanized BEC (DeGe-BEC).

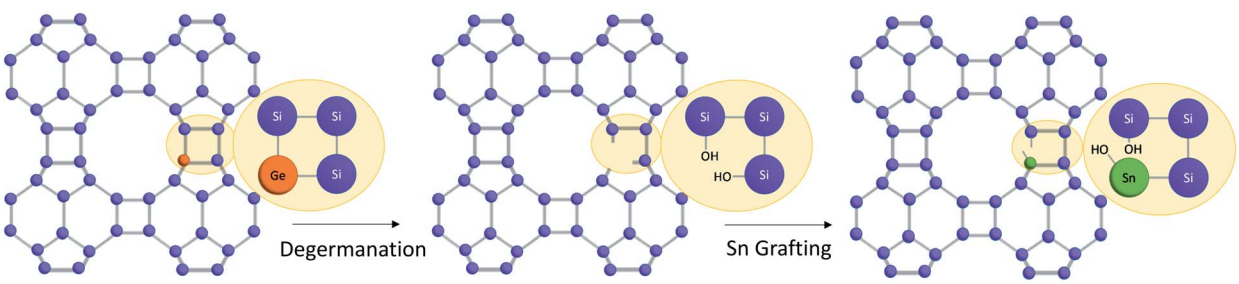

Fig. 3 Multi-step synthesis procedure to selectively place Sn in the D4Rs of high-silica BEC zeolites.

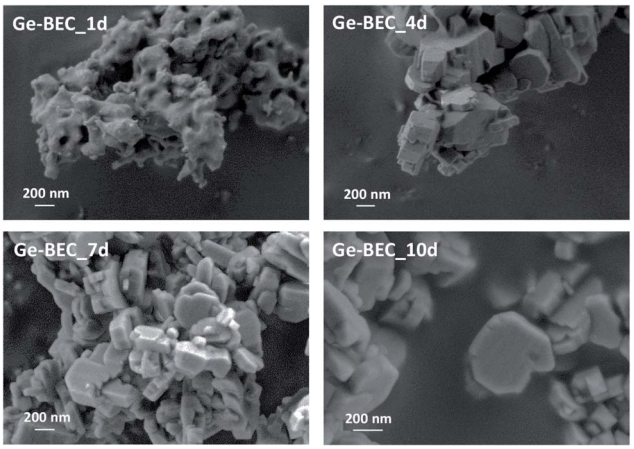

Fig. 5 FE-SEM images of the Ge-containing BEC materials after different crystallization times ranging from 1 (Ge-BEC_1d) to 10 (Ge-BEC_10d) days.

used in traditional hydrophobic Sn-Beta(F). PXRD patterns show that full crystallization of Ge-BEC is obtained after 4 days (Fig. 4) and FE-SEM micrographs indicate a homogeneous formation of BEC crystals with average particle sizes between 200–400 nm (see Fig. 5).

The chemical analyses of the four samples taken at different time points during the Ge-BEC crystallization process indicate equivalent Si/Ge molar ratios ranging between 150 and 160 for all cases (Table 1). These values are analogous to those initially incorporated in the synthesis gels (Si/Ge $\sim$ 150). The ^{19}F MAS NMR spectrum for the as-prepared Ge-BEC materials features two well-defined signals localized at -38 and -20 ppm (see Fig. 6). These signals have been assigned to fluoride species trapped within pure silica D4R units and D4R units containing one Ge atom, respectively.[42] The ratio of the integrated areas of these two peaks remains constant at $\sim$10 after 4 days of synthesis time. Considering that the number of T-sites in the D4Rs is 50% of the total T-sites per unit cell (*i.e.*, 16 of 32 T-atoms), the ^{19}F MAS NMR data translate to $\sim$0.18 Ge atoms per unit cell, which corresponds to a Si/Ge molar ratio of $\sim$170. This value is in close agreement with the value of $\sim$155 measured by bulk ICP analysis (see Table 1), suggesting that Ge atoms are exclusively incorporated in the D4Rs. The ^{29}Si MAS NMR spectrum of the as-prepared Ge-BEC_10d sample shows three signals centred at -106, -110 and -117 ppm (Fig. 7).

Table 1 ICP chemical analyses of the different zeolite samples

Sample	Si/Ge	Si/Sn	%wt Sn/TO_2
Ge-BEC_1d	163	—	—
Ge-BEC_4d	153	—	—
Ge-BEC_7d	154	—	—
Ge-BEC_10d	155	—	—
DeGe-BEC	>600	—	—
Sn-BEC	>600	330	0.60
Sn-Beta(F)	—	298	0.73

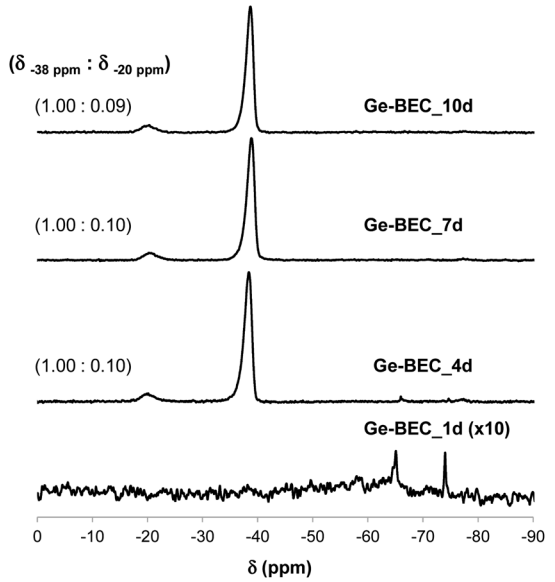

Fig. 6 ^{19}F MAS NMR spectra of the as-prepared Ge-containing BEC materials after different crystallization times. The measured signal ratios are included for all Ge-BEC samples.

These signals are assigned to Si atoms at the three distinct crystallographic T-sites in the BEC framework and show a T_1-: T_2 : T_3 ratio of 2 : 1 : 1, in good agreement with the crystallographic information of the BEC structure.

The second step in the synthesis of Sn-BEC involved the selective removal of Ge species from the BEC framework *via*

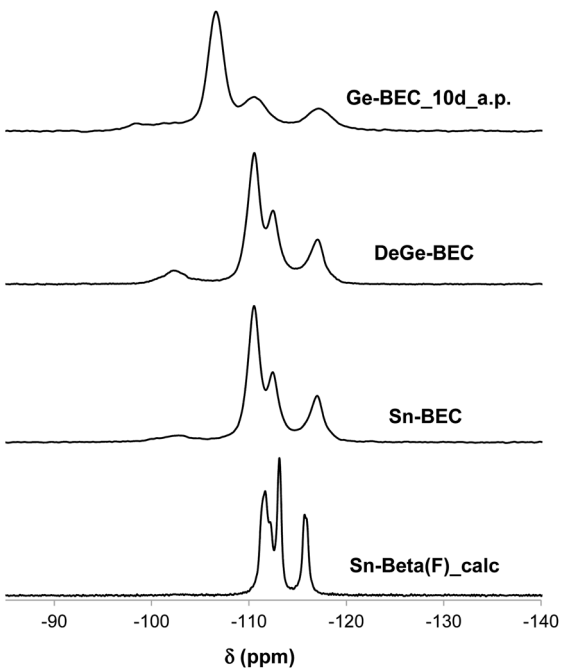

Fig. 7 ^{29}Si MAS NMR spectra of the as-prepared Ge-BEC_10d (Ge-BEC_10d_a.p.), after the degermanization process (DeGe-BEC), and after the Sn-grafting process (Sn-BEC) and ^{29}Si MAS NMR spectrum of the calcined Sn-Beta(F) (Sn-Beta(F)_calc).

sequential calcination and acid treatment. The resulting solid maintained its crystalline structure after degermanation, as revealed by PXRD (see DeGe-BEC in Fig. 4b). Chemical analysis of the treated solid indicated a Si/Ge molar ratio >600, confirming the removal of Ge from the original material (see DeGe-BEC in Table 1). The ^{29}Si MAS NMR spectrum of the degermanized sample revealed a new band centred at −103 ppm (see DeGe-BEC in Fig. 7), which can be assigned to silanol defects ($Si(OSi)_3OH$) created in the BEC structure after removal of framework Ge heteroatoms. The other ^{29}Si chemical shifts were located at −110, −112 and −117 ppm, similar to those observed in Ge-BEC (see Fig. 7). The slight differences in peak position between both samples are attributed to framework relaxation after calcination to remove the organic SDA molecules.

Sn heteroatoms were incorporated into framework defects formed by removal of Ge *via* post synthetic grafting. Specifically, methyltin(IV) trichloride was grafted into the framework vacancy defects in the D4Rs of degermanized BEC using a theoretical Si/Sn molar ratio of ∼100. Chemical analysis revealed a Si/Sn molar ratio of 330, which corresponds to ∼0.6 wt% Sn/TO_2 in the solid (see Table 1). Interestingly, the ^{29}Si MAS NMR spectrum of the Sn-BEC sample showed a substantial decrease in the signal centered at −103 ppm after the Sn grafting procedure (Fig. 7), suggesting partial healing of defect sites.

Incorporation of Sn into vacancy defects of DeGe-BEC was confirmed from UV-visible spectra measured on dehydrated Sn-BEC (Fig. 8) that show an absorption feature centered near 190 nm, which is characteristic of isolated, framework Sn atoms.[60] UV-Vis spectra of dehydrated Sn-BEC also show weak absorption features centered near 220 and 240 nm, which are absent in conventional Sn-Beta(F), and indicate the presence of extra-framework SnOx clusters, which may form as a result of incomplete grafting of lattice defects in DeGe-BEC by methyltin(IV) trichloride precursors. Collectively, these bulk spectroscopic data demonstrate that the synthetic methods described here give rise to framework Sn atoms that partially heal vacancy defects present in DeGe-BEC zeolites. Further optimization of the grafting procedure described here should lead to an increase in the specific reaction rate (per gram catalyst) by improving the efficiency of framework Sn incorporation.

3.2. Lewis acid-site characterization

Understanding the chemical and structural environments of the grafted tin species within the BEC framework is necessary to properly assess the applicability of Sn-BEC as a heterogeneous catalyst. We used two probe molecules, TMPO and CD_3CN, combined with ^{31}P MAS NMR and FTIR spectroscopies, respectively, to shed light on the atomic environment of framework tin species. Román-Leshkov *et al.* recently employed solid-state ^{31}P MAS NMR spectroscopy after adsorbing TMPO probe molecules to elucidate the identity of the Lewis acid sites in Sn-Beta (see Experimental section for details).[35] Following this approach, we observed distinct ^{31}P NMR resonance profiles for Sn-Beta(F) and Sn-BEC. At least two well-defined signals at 58.9 and 55.2 ppm appear in the ^{31}P MAS NMR spectrum of the Sn-Beta(F) zeolite with a Si/Sn molar ratio of ∼300 when using intermediate TMPO loadings (TMPO/Sn ∼ 0.5; Fig. 9).[35] In contrast, Sn-BEC presented a single ^{31}P NMR resonance centred at 59.8 ppm at a similar TMPO loading (TMPO/Sn ∼ 0.5; Fig. 9). This result suggests the presence of Lewis acid sites with a single chemical environment within the Sn-BEC crystals. Control experiments on the degermanized BEC sample, showed only a broad signal at 47.6 ppm, which could be assigned to TMPO molecules interacting with silanol groups.[61]

To correlate the experimentally observed ^{31}P NMR resonances with specific crystallographic T-sites in BEC, we carried out a detailed DFT study aimed at evaluating the interactions of TMPO with Sn atoms placed at the three distinct T-sites in BEC. Three representative T-sites in the BEA framework (T_4, T_5, and T_7; Fig. 1b) were also considered for comparison with BEC. Both

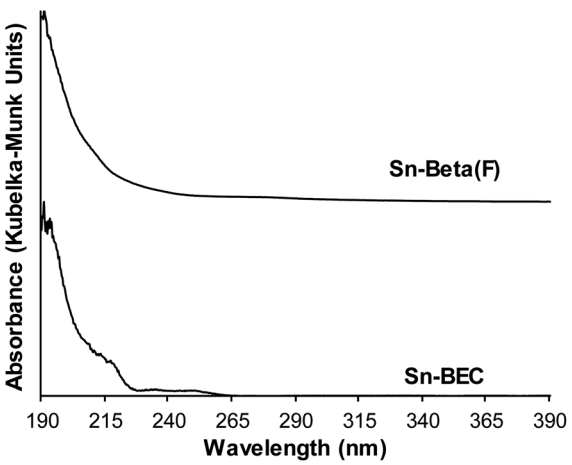

Fig. 8 UV-visible spectra of dehydrated Sn-Beta(F) (top) and Sn-BEC (lower) zeolites.

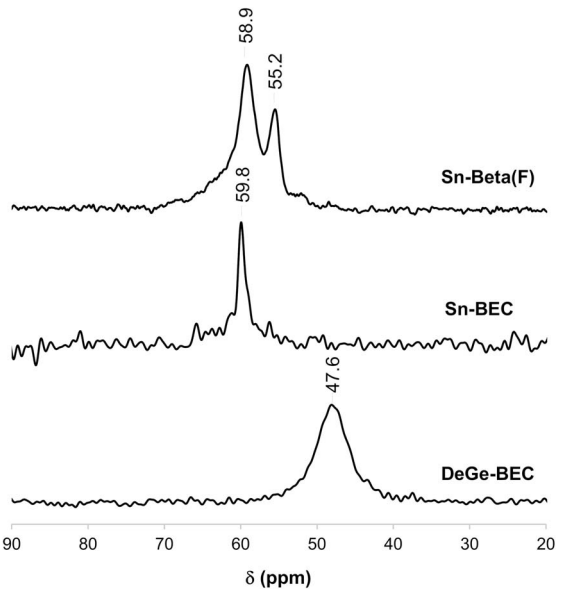

Fig. 9 ^{31}P MAS NMR spectra of TMPO dosed on DeGe-BEC, Sn-BEC and Sn-Beta(F) at P/Sn = 0.5 loading.

closed and open Sn sites were considered at all T-sites, as well as silanol groups in the two zeolite structures. TMPO adsorbs on Sn sites forming stable adducts with optimized Sn–O distances of ~2.1 Å (Fig. 10 and 11) and with the P–O bond length increasing by ~0.04 Å with respect to the optimized value for the isolated molecule in the gas phase (1.493 Å). The interaction of TMPO with silanol groups leads to less distortion of the adsorbed TMPO, with a lengthening of the P–O bond by only 0.016 Å and calculated δ ^{31}P chemical shifts of 43 and 40 ppm in BEC and BEA, respectively (Table 2).

As a result, the observed changes in the δ ^{31}P chemical shift allows the assignment of TMPO adsorbed to Sn at different T-sites. The calculated δ ^{31}P chemical shifts for TMPO interacting with Sn atoms at the T_1 and T_3 sites in Sn-BEC are similar at 61.7 and 62.3 ppm, respectively, and decrease to 60.9 and 60.2 ppm when considering open sites with a hydrolysed Sn–OH bond (see Table 2 and Fig. 10). The δ ^{31}P chemical shifts at the T_2 site are noticeably larger, 65.4 and 67.0 ppm for closed and open sites, respectively, and do not match the experimental ^{31}P MAS NMR spectrum (Fig. 9). A comparison of the calculated δ ^{31}P chemical shifts (Table 2) with the experimental ^{31}P MAS NMR spectra (Fig. 9) suggests that Sn does not occupy the T_2 position in Sn-BEC, and confirms that the experimental peak at 59.8 ppm can be mostly attributed to the placement of Sn at T_1 sites. Calculated δ ^{31}P chemical shifts indicate that Sn could also occupy T_3-OH open sites, but this possibility was excluded by ^{19}F MAS NMR data that indicate the preferential occupancy of the T_1 site by Ge and, thus, the placement of Sn at such sites.

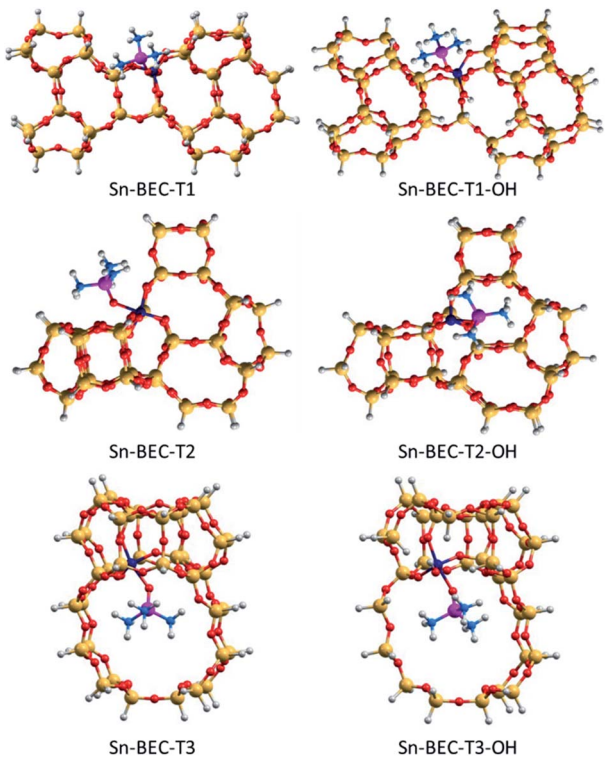

Fig. 10 DFT optimized structures of TMPO interacting with closed and open sites of Sn-BEC. Sn, Si, O, P, C and H atoms are depicted in dark blue, yellow, red, purple, blue and white, respectively.

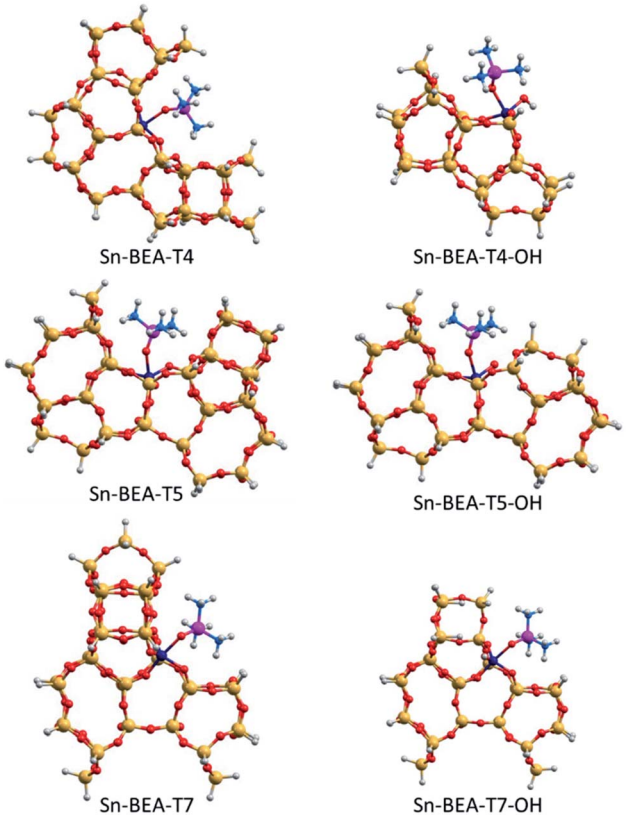

Fig. 11 DFT optimized structures of TMPO interacting with closed and open sites of Sn-BEA. Sn, Si, O, P, C and H atoms are depicted in dark blue, yellow, red, purple, blue and white, respectively.

Among the three T-sites considered within Sn-BEA (see Fig. 11), the closed sites at T_4 and T_5 lead to low δ ^{31}P chemical shifts, 54.2 and 57.2 ppm, respectively, which increase to 59.0 and 59.5 ppm, respectively, for the corresponding open sites. In contrast, the calculated δ ^{31}P chemical shifts for the open and closed Sn sites at T_7 are similar and more strongly deshielded than T_4 and T_5 (60.9 and 60.5 ppm, respectively). The calculated δ ^{31}P chemical shifts of TMPO adsorbed at just a subset of the different T-sites present in the BEA framework, which is only one of the polymorphs that comprise conventional Sn-Beta catalysts (*e.g.*, BEA and BEB), and the convolution of multiple chemical environments observed in experimental ^{31}P MAS NMR spectra (Fig. 9) highlight the complexity of assigning chemical shifts in zeolites with a wide diversity of T-sites.

Lewis acidic Sn sites were also titrated by deuterated acetonitrile (CD_3CN), a known probe molecule of open and closed Sn sites in zeolites.[36,38] IR spectra measured after adsorption of CD_3CN on Sn-containing BEC and Beta(F) zeolites at different coverages are shown in Fig. 12. At low coverages of CD_3CN in both Sn-zeolites (CD_3CN/Sn < 0.2) a single peak characteristic of CD_3CN bound to Lewis acidic open Sn sites (ν(C≡N) = 2316 cm^{-1}) is observed, which undergoes a shift in peak center with increasing coverage as CD_3CN populates Lewis acidic closed Sn sites (ν(C≡N) = 2308 cm^{-1}). This is consistent with prior work that has shown that CD_3CN preferentially binds to open Sn sites prior to coordination at other adsorption sites in

Table 2 Isotropic δ ^{31}P chemical shifts and optimized PO bond lengths calculated for TMPO interacting with different Sn sites and silanol groups in BEC and BEA

Catalyst	Site	δ ^{31}P (ppm)	r(PO) (Å)	Catalyst	Site	δ ^{31}P (ppm)	r(PO) (Å)
Sn-BEC	T_1	61.7	1.539	Sn-BEA	T_4	54.2	1.530
Sn-BEC	T_1-OH	60.9	1.537	Sn-BEA	T_4-OH	59.0	1.533
Sn-BEC	T_2	65.4	1.542	Sn-BEA	T_5	57.2	1.533
Sn-BEC	T_2-OH	67.0	1.542	Sn-BEA	T_5-OH	59.5	1.531
Sn-BEC	T_3	62.3	1.536	Sn-BEA	T_7	60.5	1.532
Sn-BEC	T_3-OH	60.2	1.532	Sn-BEA	T_7-OH	60.9	1.541
BEC	Si–OH	43.1	1.509	BEA	Si–OH	40.3	1.509

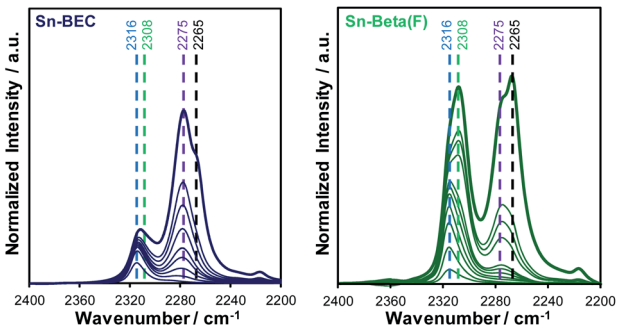

Fig. 12 FTIR difference spectra of Sn-BEC (left) and Sn-Beta(F) (right) with increasing CD_3CN coverage (0.1–0.7 μmol per dose). Dashed reference lines shown for open Sn sites (2316 cm^{-1}), closed Sn sites (2308 cm^{-1}), silanol groups (2275 cm^{-1}), and gas-phase CD_3CN (2265 cm^{-1}).

Sn-zeolites.[36,38] At higher coverages (CD_3CN/Sn > 0.3), peaks characteristic of CD_3CN bound to SiOH groups (ν(C≡N) = 2275 cm^{-1}) and physisorbed CD_3CN (ν(C≡N) = 2265 cm^{-1}) are observed.

The total number of Lewis acid sites and the ratio of open to closed Sn sites were quantified using previously reported integrated molar extinct coefficients for CD_3CN adsorbed in Sn-zeolites and these values are tabulated in Table 3.[38] The fraction of Lewis acidic Sn sites (LAS/Sn = 0.81; per total Sn) and the open/closed site ratio in Sn-Beta(F) (open/closed = 0.54) are similar to the values expected for Sn-Beta zeolites synthesized in the presence of fluoride mineralizing agents.[38] Sn-BEC contains a lower fraction of Lewis acidic Sn sites than Sn-Beta(F) (LAS/Sn = 0.47), likely reflecting the formation of extraframework SnOx clusters (Fig. 8), but contains a larger fraction of Sn in open configurations (open/closed = 1.40) than conventional Sn-Beta(F) (open/closed = 0.54) and Sn-Ge-BEC zeolites prepared *via* direct synthesis (open/closed = 0.13).[37] We hypothesize that open Sn sites are preferentially formed when Sn is post-synthetically grafted into vacancy defects of degermanated BEC zeolites. This presumably reflects the inability of Sn to match the flexibility of Ge and form four bonds to framework O atoms at the T_1 defect sites formed upon degermanation. Collectively, the spectroscopic and computational data of adsorbed probe molecules (*i.e.*, TMPO and CD_3CN) provide evidence that the synthetic methods described here place Sn atoms at well-defined sites in the BEC framework, a design strategy that is currently inaccessible in conventional Sn-Beta(F) zeolites.

Table 3 Fraction of Lewis acidic Sn sites (per mol Sn) and fraction of open/close Sn sites on Sn-BEC and Sn-Beta(F) based on FTIR difference spectra using CD_3CN as titrant

Species	Sn-BEC	Sn-Beta(F)
LAS/Sn	0.47	0.81
Open/closed	1.40	0.54

3.3. Catalytic activity: Meerwein–Ponndorf–Verley–Oppenauer (MPVO) reaction

Initial rates of the MPVO reaction, normalized per open Sn site,[21] between 2-butanol and cyclohexanone to form 2-butanone and cyclohexanol were measured on both Sn-BEC and Sn-Beta(F) as a function of cyclohexanone concentration (0.01–1 M) in a 2-butanol solvent at 100 °C (Fig. 13). Cyclohexanol formation rates (per open Sn) on both samples increase linearly at low cyclohexanone concentrations (<0.1 M) before levelling off and

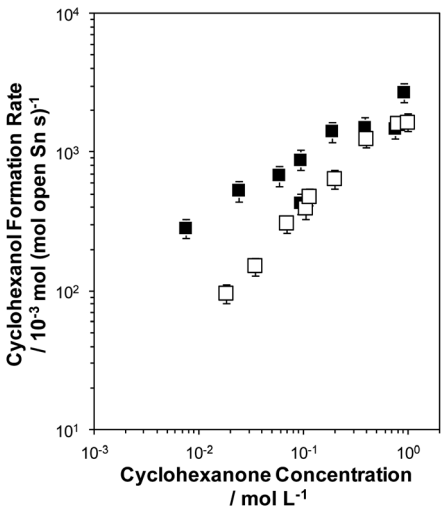

Fig. 13 Cyclohexanol formation rates (100 °C, per open Sn site) measured on Sn-BEC (solid squares) and Sn-Beta(F) (open squares) zeolites. Error bars represent propagated experimental uncertainty.

approaching a zero-order kinetic regime at higher concentrations of cyclohexanone (>0.5 M). At low cyclohexanone concentrations, cyclohexanol formation rates are ~3–4× larger on Sn-BEC than on Sn-Beta(F), but become similar (within 1.5×) at high cyclohexanone concentrations in the zero-order regime (>0.5 M). These data indicate that first-order free energy barriers, which reflect differences in free energy between the MPVO transition state and solution phase cyclohexanone and the 2-butanol covered site,[21,62] are smaller in Sn-BEC than in Sn-Beta(F). Zero-order free energy barriers, which reflect free energy differences between the MPVO transition state and the co-adsorbed 2-butanol-cyclohexanone precursor,[21] however, appear to be similar in both Sn-BEC and Sn-Beta(F) and suggest that adsorbed intermediates and the transition state they form are solvated to similar extents by the BEC and Beta frameworks. Additionally, these data indicate that cyclohexanone adsorption is likely more favourable in Sn-BEC than in Sn-Beta(F), under the conditions investigated here (2-butanol solvent, 100 °C), as differences in first-order rates reflect differences in the coupled free energy barriers of both adsorption and transition state formation. We surmise that this difference in the first-order free energy barrier reflects the preferential stabilization of the adsorbed cyclohexanone intermediate within the Sn-BEC framework due to stronger van der Waals interactions between the adsorbed species and the cylindrical BEC pore (~0.7 nm in diameter), which is smaller in diameter than stacking faults present in Sn-Beta zeolites (~1–1.5 nm)[40] that preferentially form open Sn sites.[37] This observation further highlights how turnover rates of reactions catalyzed by Lewis acidic zeolites are not dictated solely by the nature of the active site (*e.g.*, open or closed Sn coordination), but also by the secondary solvating environment that confine such sites.[63] Ultimately, these data demonstrate that open Sn sites incorporated at the T_1 site in the BEC framework act as Lewis acid sites that facilitate catalytic turnover of MPVO reactions and give rise to turnover frequencies (normalized per open Sn site) comparable to conventional Sn-Beta(F) zeolites, but higher specific rates due to the higher proportion of open sites per catalyst mass.

4. Conclusions

Sn-BEC zeolites were successfully synthesized with Sn atoms positionally biased into the D4R of the BEC framework *via* post-synthetic grafting of Sn into degermanated Ge-BEC zeolites containing low concentrations of Ge in the starting framework (Si/Ge = 155). ^{19}F and ^{29}Si MAS NMR spectra revealed the preferential incorporation of Ge atoms into the D4R secondary building unit of the BEC framework and showed that silanol defect sites ($Si(OSi)_3$–OH), which serve as grafting sites for reactive Sn precursors, form upon degermanation after treatment under mild acid (0.1 M HCl). ^{31}P MAS NMR and DFT calculations of TMPO adsorbed within Sn-BEC (TMPO/Sn = 0.5) revealed distinct chemical shifts for TMPO adsorbed at open and closed Sn sites and at the three distinct T-sites in BEC. These data indicate that Sn atoms are predominantly incorporated at the T_1 site of the BEC framework and IR spectra of adsorbed CD_3CN, a known titrant of open and closed Sn sites in zeolites, revealed the preferential formation of open Sn sites after post-synthetic grafting of Sn into degermanated BEC zeolites. Rates of the MPVO reaction between 2-butanol and cyclohexanone (normalized per open Sn site, 100 °C) measured on Sn-BEC are comparable to those measured on a conventional Sn-Beta(F) zeolite and show a similar kinetic dependence on cyclohexanone concentration, confirming the formation of catalytically active Sn sites in Sn-BEC. The data presented here highlight synthetic techniques that utilize sacrificial heteroatoms to selectively position catalytic active sites at specific T-sites within a given zeolite framework and demonstrate a method to control the location of adsorption and catalytic active sites in zeolites with atomic precision.

Conflicts of interest

There are no conflicts to declare.

Acknowledgements

This work has been supported by the Spanish Government-MINECO through "Severo Ochoa" (SEV-2016-0683), MAT2017-82288-C2-1-P (AEI/FEDER, UE) and RTI2018-101033-B-I00 (MCIU/AEI/FEDER, UE), and by Generalitat Valenciana through AICO/2019/060. JRD and YR-L thank the U.S. Department of Energy, Office of Basic Energy Sciences under Award No. DE-SC0016214 for support. ARF acknowledges the Spanish Government-MINECO for a FPU scholarship (FPU2017/01521). The Electron Microscopy Service of the UPV is acknowledged for their help in sample characterization.

Notes and references

1 B. C. Knott, C. T. Nimlos, D. J. Robichaud, M. R. Nimlos, S. Kim and R. Gounder, *ACS Catal.*, 2018, **8**, 770–784.
2 J. Dědeček, E. Tabor and S. Sklenak, *ChemSusChem*, 2019, **12**, 556–576.
3 J. Chen, T. Liang, J. Li, S. Wang, Z. Qin, P. Wang, L. Huang, W. Fan and J. Wang, *ACS Catal.*, 2016, **6**, 2299–2313.
4 A. B. Pinar, C. Márquez-Álvarez, M. Grande-Casas and J. Pérez-Pariente, *J. Catal.*, 2009, **263**, 258–265.
5 A. B. Pinar, L. Gómez-Hortigüela, L. B. McCusker and J. Pérez-Pariente, *Chem. Mater.*, 2013, **25**, 3654–3661.
6 Y. Román-Leshkov, M. Moliner and M. E. Davis, *J. Phys. Chem. C*, 2011, **115**, 1096–1102.
7 T. Biligetu, Y. Wang, T. Nishitoba, R. Otomo, S. Park, H. Mochizuki, J. N. Kondo, T. Tatsumi and T. Yokoi, *J. Catal.*, 2017, **353**, 1–10.
8 E. M. Gallego, C. Li, C. Paris, N. Martín, J. Martínez-Triguero, M. Boronat, M. Moliner and A. Corma, *Chem.–Eur. J.*, 2018, **24**, 14631–14635.
9 C. Li, A. Vidal-Moya, P. J. Miguel, J. Dedecek, M. Boronat and A. Corma, *ACS Catal.*, 2018, **8**, 7688–7697.
10 T. Yokoi, H. Mochizuki, S. Namba, J. N. Kondo and T. Tatsumi, *J. Phys. Chem. C*, 2015, **119**, 15303–15315.

11 J. R. Di Iorio and R. Gounder, *Chem. Mater.*, 2016, **28**, 2236–2247.
12 M. L. Sarazen, E. Doskocil and E. Iglesia, *J. Catal.*, 2016, **344**, 553–569.
13 A. J. Jones, R. T. Carr, S. I. Zones and E. Iglesia, *J. Catal.*, 2014, **312**, 58–68.
14 P. M. Kester, J. T. Miller and R. Gounder, *Ind. Eng. Chem. Res.*, 2018, **57**, 6673–6683.
15 T. Liang, J. Chen, Z. Qin, J. Li, P. Wang, S. Wang, G. Wang, M. Dong, W. Fan and J. Wang, *ACS Catal.*, 2016, **6**, 7311–7325.
16 C. Márquez-Alvarez, A. B. Pinar, R. García, M. Grande-Casas and J. Pérez-Pariente, *Top. Catal.*, 2009, **52**, 1281–1291.
17 E. M. Gallego, M. T. Portilla, C. Paris, A. León-Escamilla, M. Boronat, M. Moliner and A. Corma, *Science*, 2017, **355**, 1051–1054.
18 C. Li, C. Paris, J. Martínez-Triguero, M. Boronat, M. Moliner and A. Corma, *Nat. Catal.*, 2018, **1**, 547–554.
19 B. Notari, *Adv. Catal.*, 1996, **41**, 253–334.
20 A. Corma, L. T. Nemeth, M. Renz and S. Valencia, *Nature*, 2001, **412**, 423–425.
21 M. Boronat, A. Corma and M. Renz, *J. Phys. Chem. B*, 2006, **110**, 21168–21174.
22 A. Corma, S. Iborra and A. Velty, *Chem. Rev.*, 2007, **107**, 2411–2502.
23 Y. Román-Leshkov and M. E. Davis, *ACS Catal.*, 2011, **1**, 1566–1580.
24 M. Moliner, *Dalton Trans.*, 2014, **43**, 4197–4208.
25 A. Corma and M. Renz, *Chem. Commun.*, 2004, 550–551.
26 O. de la Torre, M. Renz and A. Corma, *Appl. Catal., A*, 2010, **380**, 165–171.
27 Y. Román-Leshkov, M. Moliner, J. A. Labinger and M. E. Davis, *Angew. Chem., Int. Ed.*, 2010, **49**, 8954–8957.
28 W. R. Gunther, Y. Wang, Y. Ji, V. K. Michaelis, S. T. Hunt, R. G. Griffin and Y. Román-Leshkov, *Nat. Commun.*, 2012, **3**, 1109.
29 J. Dijkmans, W. Schutyser, M. Dusselier and B. F. Sels, *Chem. Commun.*, 2016, **52**, 6712–6715.
30 R. Gounder and M. E. Davis, *J. Catal.*, 2013, **308**, 176–188.
31 M. A. Camblor, A. Corma and S. Valencia, *Chem. Commun.*, 1996, 2365.
32 R. Martínez-Franco, C. Paris, M. E. Martínez-Armero, C. Martínez, M. Moliner and A. Corma, *Chem. Sci.*, 2016, **7**, 102–108.
33 M. M. J. Treacy and J. M. Newsam, *Nature*, 1988, **332**, 249–251.
34 S. R. Bare, S. D. Kelly, W. Sinkler, J. J. Low, F. S. Modica, S. Valencia, A. Corma and L. T. Nemeth, *J. Am. Chem. Soc.*, 2005, **127**, 12924–12932.
35 J. D. Lewis, M. Ha, H. Luo, A. Faucher, V. K. Michaelis and Y. Román-Leshkov, *ACS Catal.*, 2018, **8**, 3076–3086.
36 M. Boronat, P. Concepcion, A. Corma, M. Renz and S. Valencia, *J. Catal.*, 2005, **234**, 111–118.
37 J. S. Bates, B. C. Bukowski, J. W. Harris, J. Greeley and R. Gounder, *ACS Catal.*, 2019, **9**, 6146–6168.
38 J. W. Harris, M. J. Cordon, J. R. Di Iorio, J. C. Vega-Vila, F. H. Ribeiro and R. Gounder, *J. Catal.*, 2016, **335**, 141–154.
39 J. M. Newsam, M. M. J. Treacy, W. T. Koetsier and C. B. De Gruyter, *Proc. R. Soc. London, Ser. A*, 1988, **420**, 375–405.
40 P. A. Wright, W. Zhou, J. Pérez-Pariente and M. Arranz, *J. Am. Chem. Soc.*, 2005, **127**, 494–495.
41 A. Corma, M. T. Navarro, F. Rey, J. Rius and S. Valencia, *Angew. Chem., Int. Ed.*, 2001, **40**, 2277–2280.
42 G. Sastre, J. A. Vidal-Moya, T. Blasco, J. Rius, J. L. Jordá, M. T. Navarro, F. Rey and A. Corma, *Angew. Chem., Int. Ed.*, 2002, **41**, 4722–4726.
43 G. Zhang, P. Feng, W. Zhang, H. Liu, C. Wang, H. Ma, D. Wang and Z. Tian, *Microporous Mesoporous Mater.*, 2017, **247**, 158–165.
44 A. Rodríguez-Fernández, F. J. Llopis, C. Martínez, M. Moliner and A. Corma, *Microporous Mesoporous Mater.*, 2018, **267**, 35–42.
45 P. Eliášová, M. Opanasenko, P. S. Wheatley, M. Shamzhy, M. Mazur, P. Nachtigall, W. J. Roth, R. E. Morris and J. Čejka, *Chem. Soc. Rev.*, 2015, **44**, 7177–7206.
46 A. Rodríguez-Fernández, P. Atienzar, C. Martínez, Y. Román-Leshkov and M. Moliner, *Chem. Mater.*, 2019, **31**, 7723–7731.
47 M. Moliner, P. Serna, Á. Cantín, G. Sastre, M. J. Díaz-Cabanas and A. Corma, *J. Phys. Chem. C*, 2008, **112**, 19547–19554.
48 Á. Cantín, A. Corma, M. J. Díaz-Cabañas, J. L. Jordá, M. Moliner and F. Rey, *Angew. Chem., Int. Ed.*, 2006, **45**, 8013–8015.
49 J. D. Lewis, S. Van de Vyver and Y. Román-Leshkov, *Angew. Chem., Int. Ed.*, 2015, **54**, 9835–9838.
50 R. Bermejo-Deval, M. Orazov, R. Gounder, S.-J. Hwang and M. E. Davis, *ACS Catal.*, 2014, **4**, 2288–2297.
51 Y. Zhao and D. G. Truhlar, *Theor. Chem. Acc.*, 2008, **119**, 525.
52 R. Ditchfield, W. J. Hehre and J. A. Pople, *J. Chem. Phys.*, 1971, **54**, 724–728.
53 W. J. Hehre, R. Ditchfield and J. A. Pople, *J. Chem. Phys.*, 1972, **56**, 2257–2261.
54 P. J. Hay and W. R. Wadt, *J. Chem. Phys.*, 1985, **82**, 270–283.
55 P. J. Hay and W. R. Wadt, *J. Chem. Phys.*, 1985, **82**, 299–310.
56 M. J. Frisch, G. W. Trucks, H. B. Schlegel, G. E. Scuseria, M. A. Robb, J. R. Cheeseman, G. Scalmani, V. Barone, B. Mennucci, G. A. Petersson, H. Nakatsuji, M. Caricato, X. Li, H. P. Hratchian, A. F. Izmaylov, J. Bloino, G. Zheng, J. L. Sonnenberg, M. Had and D. J. Fox, *Gaussian 09.*, Gaussian, Inc., Wallingford, CT, 2009.
57 R. Ditchfield, *Mol. Phys.*, 1974, **27**, 789–807.
58 K. Wolinski, J. F. Hinton and P. Pulay, *J. Am. Chem. Soc.*, 1990, **112**, 8251–8260.
59 A. D. McLean and G. S. Chandler, *J. Chem. Phys.*, 1980, **72**, 5639–5648.
60 M. Moliner, Y. Román-Leshkov and M. E. Davis, *Proc. Natl. Acad. Sci. U. S. A.*, 2010, **107**, 6164–6168.
61 A. Zheng, S.-B. Liu and F. Deng, *Chem. Rev.*, 2017, **117**, 12475–12531.
62 H. Y. Luo, D. F. Consoli, W. R. Gunther and Y. Román-Leshkov, *J. Catal.*, 2014, **320**, 198–207.
63 J. W. Harris, J. S. Bates, B. C. Bukowski, J. Greeley and R. Gounder, *ACS Catal.*, 2020, **10**, 9476–9495.